ACS OMEGA

http://pubs.acs.org/journal/acsodf

Article

Erythrocyte−Cancer Hybrid Membrane-Camouflaged Prussian Blue Nanoparticles with Enhanced Photothermal Therapy in Tumors

Zhining Liu, Huichao Xie,* and Tianyi Wang*

Cite This: *ACS Omega* 2023, 8, 23056−23066

Read Online

ACCESS | Metrics & More | Article Recommendations

ABSTRACT: Prussian blue (PB) nanoparticles have been widely used in photothermal therapy research due to the efficient photothermal conversion ability. In this study, PB was modified with a bionic coating using a hybrid membrane of red blood cell membranes and tumor cell membranes to prepare bionic photothermal nanoparticles (PB/RHM), which can further improve the blood circulation ability and tumor targeting of the nanoparticles to achieve efficient photothermal therapy for tumor treatment. *In vitro* formulation characterization showed that PB/RHM was a monodisperse spherical core−shell structured nanoparticle with a diameter of 207.2 nm and effectively retained the cell membrane proteins. The *in vivo* biological evaluation results showed that PB/RHM could effectively accumulate into the tumor tissue, inducing a rapid temperature increase in the tumor site to 50.9 °C within 10 min, inhibiting tumor growth efficiently with a tumor inhibition rate of 93.56% and with good therapeutic safety. In summary, this paper provided a hybrid film-modified Prussian blue nanoparticle with efficient photothermal anti-tumor capacity and safety.

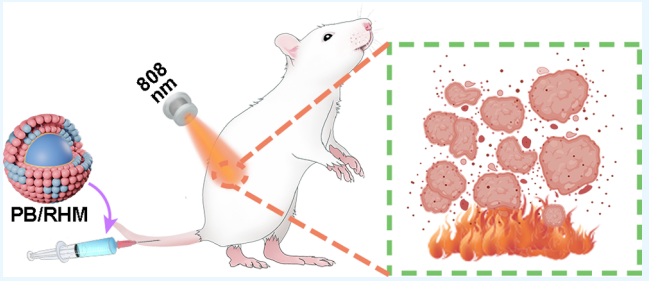

INTRODUCTION

Developing promising cancer treatment strategies is a matter of urgency. The unavoidable side effects of traditional oncology treatments such as chemotherapy, radiotherapy, and surgery cause great suffering to patients.[1] Based on the development of nanotechnology, nanoplatform provides a perfect loading and transport platform for targeted delivery and intelligent release of drugs such as small molecules, genes, peptides, inorganic materials, and therapeutic gases, which can effectively increase the targeted accumulation efficiency, improve pharmacokinetic properties, and reduce toxic effects of drugs.[2−7] Gentle and noninvasive treatments have attracted a lot of attention due to their effective tumor-destroying ability and minimal harm to normal tissues.[8] Photothermal therapy (PTT) has become an important research direction in anti-tumor research because of its safety, efficiency, and on-demand modifiability.[9−11]

Prussian blue (PB), a pigment with a long history of application, is now widely used in modern medical research for photothermal therapy and medical imaging.[12] Prussian blue nanoparticle is a classical hexacyanoferrate with a crystal skeleton of Fe(II)-C≡N-Fe(III), with Fe^{3+} linked to the N atom and Fe^{2+} linked to the C atom in the cyanide group, arranged alternately to form a cubic crystal.[13−15] The efficient photothermal conversion capability is due to the stretching vibrations of the C≡N coordination bond bridge in its structural unit with strong absorption in the first window region of 600−900 nm NIR light.[16] Compared with other photothermal agents, Prussian blue nanoparticles have the advantages of a simple preparation process, common and inexpensive synthesis materials, ease of control of the nano size and microscopic morphology, mesoporous structure of drug loading, surface modification and functionalization, and good photothermal stability.[17−19]

Avoiding phagocytic clearance of nanomedicines in the circulatory system and achieving efficiently targeted accumulation in tumor areas are key issues that must be addressed in order to achieve the clinical application of nanomedicines.[19] The "top-down" endogenous biofilm bionanomimetic coating strategy for direct functional endowment of nanoparticles is an emerging solution.[20] The cell membranes used in the current research reports mainly include erythrocyte membranes, platelet membranes, immune cell membranes, tumor cell membranes, organelle membranes, bacterial cell membranes, and hybrid membranes, in which the hybrid membrane system of erythrocyte and tumor cell membranes is an important branch of the research.[21] The key strategic advantages include (1) the ability to obtain blood circulation invisibility by means of self-recognition communication between the erythrocyte

Received: April 8, 2023
Accepted: May 26, 2023
Published: June 9, 2023

https://doi.org/10.1021/acsomega.3c02370
ACS Omega 2023, 8, 23056−23066

membrane protein CD47 and phagocytes; (2) tumor-specific homing/targeting properties of the nanoparticles conferred by the tumor cell membrane; (3) natural biocompatibility, friendly to both the blood system and tissue and organs; (4) stabilization and isolation of the nanoparticles, avoiding direct contact between the nanoparticles and the blood system; and (5) antigenic antigens of tumor cell membranes can stimulate the immune system to enhance tumor-specific immune responses.[22−26]

In this manuscript, our study was to camouflage and modify the Prussian blue nanoparticles by using a hybrid membrane of red blood cell membrane (RBCM) and tumor cell membrane as a bionic shell, improving the blood long circulation ability and tumor-targeting ability of the photothermal nanoparticles and increasing the accumulation concentration in the tumor region, thus improving the sensitivity of photothermal therapy and promoting the thermal damage effect on the tumor.

EXPERIMENTAL SECTION

Materials. Povidone K30 (PVP K30) was purchased from BASF SE (Ludwigshafen, Germany). Potassium ferricyanide ($K_3[Fe(CN)_6]$), sodium ethylenediaminetetraacetic acid 2 (EDTA-2Na), and phosphate-buffered saline (PBS) were all obtained from Shanghai Yuanye Bio-Technology Co., Ltd. (Shanghai, China). Bicinchoninic acid (BCA) Protein Assay Kit, Membrane and Cytosol Protein Extraction Kit, phenylmethylsulfonyl fluoride protease inhibitors (PMSF), 1,1″-dioctadecyl-3,3,3″,3″-tetramethylindotricarbocyanine iodide (DiR), 3,3′-dioctadecyloxacarbocy-anine perchlorate (DiO), 2″-(4-ethoxyphenyl)-5-(4-methylpiperazin-1-yl)-2,5′-bibenzimidazole (Hoechst 33342), PI, Coomassie brilliant blue, and anti-fluorescent quenching agent were all purchased from Beyotime Institute of Biotechnology (Shanghai, China). Roswell park memorial institute (RPMI 1640) medium and fetal bovine serum (FBS) were all purchased from Corning, Inc. (New York). Hematoxylin and eosin (HE) staining kit, TdT-mediated dUTP nick-end labeling (TUNEL) apoptosis detection kit (Alexa Fluor 640), Ki67 Cell Proliferation Kit (IF), and FITC anti-mouse CD31 antibody (FITC-CD31) were all purchased from Roche (Basel, Switzerland).

Methods. *Preparation of PB.* PVP K30 (5 g) was dissolved in HCl solution (1 M, 40 mL), and 396 mg of $K_3[Fe(CN)_6]$ was then added and stirred magnetically for 30 min to form a clear yellow solution. The solution was transferred to a round-bottom flask and aged for 20 h at 80 °C. At the end of the reaction, the system was cooled to room temperature; 80 mL of acetone was added and centrifuged at 15,000 rpm for 20 min. The supernatant was discarded, and the blue precipitated layer was resuspended in ethanol, centrifuged at 15,000 rpm for 60 min, and washed twice. The blue precipitated layer was washed twice with deionized water and then lyophilized to obtain Prussian blue (PB) nanoparticles. PB lyophilized powder can be used by resuspension in deionized water or normal saline, depending on the experimental needs.

Preparation of RBCM. Erythrocyte membranes were prepared with reference to a published protocol.[27] Briefly, the female KM mice had their whiskers clipped and the eye area cleaned; then, the eyeball was removed to obtain whole blood, and an appropriate amount of EDTA-2Na solution (3.2%, w/v) was added as an anticoagulant. The blood was centrifuged at 2800 rpm for 10 min. The upper plasma layer and the middle layer of platelets and leukocytes were carefully removed, and the bottom layer of red blood cells was collected. The erythrocytes were washed twice with cold PBS solution (containing 1% PMSF, v/v) and then resuspended in deionized water containing 0.2 mM EDTA-2Na and subjected to hypotonic treatment for 60 min. Afterward, the hemoglobin was removed by centrifugation at 15,000 rpm for 20 min, and the precipitated layer was collected. The hypotonic operation was repeated once under the same conditions. The obtained precipitated layer was repeatedly washed with cold PBS solution (containing 1% PMSF, v/v) to a colorless supernatant, and the pure red blood cell membrane (RBCM) was prepared. All of the above operations were carried out at 4 °C in order to preserve the structural and functional properties of the membrane proteins. The RBCM suspension was quantified by the BCA kit protein and stored in liquid nitrogen.

Preparation of H22M. 1×10^6 of H22 cells were injected into the peritoneal cavity of KM mice and fed normally for 5−7 days to obtain a sufficient amount of ascites tumor cell suspensions. Ascites was extracted using a sterile syringe, H22 cells were collected by centrifugation at 1400 rpm, and the cell membranes were lysed using a Membrane and Cytosol Protein Extraction Kit combined with probe ultrasound (5 W, 2 min, Ultrasonic Processor JY92-IIN, Scientz, China). After centrifugation at 3200 rpm for 10 min, the supernatant was carefully aspirated and further centrifuged at 15,000 rpm for 20 min. The supernatant was discarded, and the white precipitated layer was the H22 cell membrane (H22M). The H22M was resuspended in an appropriate amount of PBS (containing 1% PMSF, v/v), quantified by the BCA kit protein, and stored in liquid nitrogen.

Preparation of PB/RHM. The mass ratio of phospholipid membranes to membrane proteins in cell membranes is approximately 2:1, from which the concentration of phospholipid membranes can be deduced from the protein quantification results of BCA.[23] Based on the BCA results, RBCM equivalent to 1.25 mg of phospholipid membrane, H22M equivalent to 1.25 mg of phospholipid membrane, and 1 mg of PB were taken, and the total volume was adjusted to 2 mL by deionized water. The mass ratio of total phospholipid film to PB was 2.5:1. The mixed systems were sonicated in an ice bath using probe ultrasound at gradient intensities (50 W, 2 s on, 5 s off, 10 min; 37.5 W, 2 s on, 5 s off, 5 min; 25 W, 2 s on, 5 s off, 5 min;). Subsequently, the precipitated layer was collected by centrifugation at 10,000 rpm for 20 min, resuspended using deionized water or saline, and further sonicated (25 W, 2 s on, 5 s off, 5 min) to obtain a clear blue aqueous dispersion of PB/RHM nanoparticles.

Characterization. Malvern nanoparticle sizer based on dynamic light scattering (DLS) technology was used to determine the particle size, ζ-potential, and polydispersity index (PDI) of PB and PB/RHM at the same dilution ratio. PB/RHM aqueous dispersions were adjusted using deionized water (equivalent PB concentration: 200 μg/mL), placed in EP tubes, and allowed to stand at 4 °C in a sealed environment protected from light. On days 0, 1, 3, 10, and 21, the colloidal stability of the formulations was measured and evaluated. The dispersions of PB and PB/RHM in deionized water were deposited on the carbon film, dried naturally, and then observed by field emission transmission electron microscopy (TEM) for two-dimensional (2D) micromorphology and core−shell structure of the nanoparticles. Sodium dodecyl sulfate polyacrylamide gel electrophoresis (SDS-PAGE) experiments were used to evaluate the transfer of membrane proteins to lipid membranes. RBCM, H22M, and PB/RHM were mixed

https://doi.org/10.1021/acsomega.3c02370
ACS Omega 2023, 8, 23056−23066

with SDS sample loading buffer and heated for 3 min at 90 °C. Afterward, all samples were aliquoted on 10% SDS-PAGE gels and electrophoresed for 2 h at 100 V in constant pressure mode. The gels were quickly stained using Thomas Brilliant Blue solution and repeatedly washed with deionized water until there was no background color with clear bands. The above characterization experiments were carried out in parallel on three samples at 25 °C.

Hemolysis Assay. Whole blood was obtained from KM mice after the removal of the eyeball, and red blood cells were separated by low-temperature centrifugation and washed twice in cold sterile saline. 250 μL of RBC suspension was mixed separately with a graded concentration of nanoparticle aqueous dispersion in sterile EP tubes; the final concentration of RBC was 2% (v/v). The concentration of PB and PB/RHM (equivalent PB concentration) was 50, 75, 100, 125, 150, and 200 μg/mL, respectively. In addition, the NS group was used as a negative control (0% hemolysis), and the deionized water group was used as a positive control (100% hemolysis). The co-incubated system was incubated for 12 h at 37 °C and centrifuged at 2800 rpm for 10 min. Afterward, 300 μL of the supernatant was transferred to a new EP tube and centrifuged at 15,000 rpm for 30 min. 200 μL of the supernatant was pipetted into a 96-well plate, and the absorbance at 540 nm was measured using a multifunctional enzyme marker. Three parallel samples were set up for each group. The hemolysis rate was calculated by the following eq 1:

$$\text{hemolysis ratio (\%)} = (A_{\text{preparation}} - A_{\text{NS}})/(A_{\text{deionized water}} - A_{\text{NS}}) \times 100 \quad (1)$$

In Vitro Evaluation of the Photothermal Properties of PB and PB/RHM. A fiber-coupled laser (wavelength 808 nm, MW-GX-808/5000 mW, Changchun Femtosecond Technology Co., Ltd.) was used as the NIR light source for the entire photothermal performance test. 1 mL of nanoparticle aqueous dispersions were individually loaded into plastic cuvettes, and all samples were irradiated with the NIR laser for 5 min, during which the dynamic temperature monitoring was visualized using a thermal imager (FLIR ONE PRO, Teledyne FLIR). At 1.25 W/cm^2 light density, the photothermal temperature rise curves of PB and PB/RHM aqueous dispersions were compared and recorded at gradient concentrations (equivalent PB concentration: 50, 75, 100, 125, 150, 200 μg/mL). At an equivalent PB concentration of 100 μg/mL, the temperature rise curves of PB and PB/RHM aqueous dispersions at gradient light densities (0.5, 0.75, 1.0, 1.25, 1.5, 1.75, 2.0 W/cm^2) were compared and recorded. 1 mL of normal saline received no laser radiation and was set up as a blank group and recorded as NS(−). 1 mL of natural saline received laser radiation (1.25 W/cm^2) and was recorded as NS(+). To examine the photothermal stability, aqueous dispersions of PB and PB/RHM (equivalent PB concentration: 100 μg/mL) were irradiated with a NIR laser (1.25 W/cm^2) for 4 cycles (5 min radiation, 25 min cooling), and the resulting temperature changes during irradiation and cooling were recorded in real time, respectively.

In Vitro Cellular Uptake. Mice hepatoma 22 (H22) cells were purchased from the Shanghai Institute of Cell Biology (Shanghai, China). H22 cells were cultured at 37 °C in a 5% CO_2 humidified incubator with RPMI 1640 as the medium. Cells were incubated and collected according to standard procedures for the experiment. The lipophilic membrane dye DiO was used to label phospholipid membranes for fluorescence visualization in *in vitro* cell uptake assays. 1.6 mL of H22 cell suspension (2 × 10^5 cells) was mixed with 0.4 mL of PB/RHM-DiO in a 6-well plate and incubated for 12 h at 37 °C. The final concentration of PB/RHM-DiO was equivalent to PB 100 μg/mL. After co-incubation, the H22 cell suspension was collected into 2 mL EP tubes and centrifuged at 1400 rpm for 4 min. The cell sediment layer was washed twice with complete medium to remove free PB/RHM-DiO. 1 mL of 4% paraformaldehyde was added, and the cells were fixed at room temperature and protected from light for 30 min. The cell suspension was centrifuged at 1400 rpm for 4 min, the supernatant was discarded, and PBS solution containing Hoechst 33342 (10 μg/mL) was added and incubated for 10 min protected from light. The supernatant was discarded by centrifugation, and the cells were resuspended by adding 50 μL of anti-fluorescence quencher. An appropriate amount of cell suspension was aspirated and added dropwise to the carrier slides to prepare observation slides for visualization of cell uptake using an LSM710 confocal laser scanning microscope (Leica, Heidelberg, Germany).

PTT-Induced Tumor Ablation In Vitro. H22 cells were used to evaluate the photothermal damage of tumor cells induced by the exposure of PB/RHM to light radiation. For *in vitro* photothermal treatment, 1.6 mL of H22 cell suspension (2 × 10^5 cells) was mixed with 0.4 mL of PB or PB/RHM dispersion in 6-well plates and incubated for 12 h at 37 °C, respectively. The final concentration of PB/RHM was equivalent to PB 100 μg/mL. After co-incubation, the H22 cell suspension was collected into 2 mL EP tubes and centrifuged at 1400 rpm for 4 min. Complete medium was used to wash the cells twice. H22 cells were resuspended in complete medium and subjected to photothermal treatment (808 nm, 1.25 W/cm^2) for 10 min. Following the photothermal treatment, the cell suspension was left to stand at 37 °C to restore the cell state. The cells were collected by centrifugation at 1400 rpm for 4 min after 1 h. The cells were fixed in 4% paraformaldehyde solution for 30 min and washed in PBS. PBS solution containing Hoechst 33343 (10 μg/mL), and PI (50 μg/mL) was added to stain the cells for 20 min, and the cells were washed with PBS. The supernatant was discarded by centrifugation, and the cells were resuspended by adding 50 μL of anti-fluorescence quencher. An appropriate amount of cell suspension was aspirated and added dropwise to the carrier slides to prepare observation slides for visualization using an inverted fluorescence microscope (IXT3, Olympus Corporation, Osbalin, Japan).

Establishment of the H22 Tumor Model. The H22 ectopic tumor model was established by subcutaneous injection of 100 uL of ascites containing H22 cells (2 × 10^6 cells per mouse) into the right hind side of female KM mice (18−20 g). All animals in the study were purchased from Jinzhou Medical University (Shenyang, Liaoning, China); the relevant animal protocols were reviewed and approved by the Animal Care and Use Committee of Jinzhou Medical University, and the ethics number was 2023018. The growth size of the tumor was measured by digital vernier calipers and calculated by the following eq 2:

$$\text{volume (mm}^3\text{)} = [\text{length} \times (\text{width})^2]/2 \quad (2)$$

In Vivo Targeting Tumor Evaluation. To evaluate the active tumor-targeting ability of the RHM-coated incubated

https://doi.org/10.1021/acsomega.3c02370
ACS Omega 2023, 8, 23056−23066

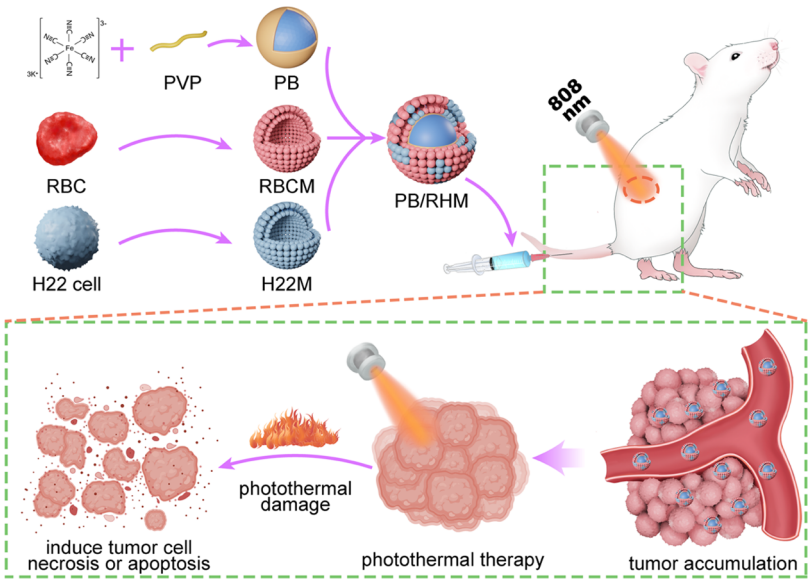

Figure 1. Schematic illustration of the preparation and mechanism of action of the bionic photothermal nano-delivery system (PB/RHM).

formulation, the lipid-soluble membrane dye DiR was labeled with the RHM coating to enable visual tracking of PB/RHM. When the H22 tumor volume increased to 300 mm^3, mice were injected with PB/RHM (equivalent PB: 5 $\mu g/g$ body weight) via the caudal vein. Three mice were randomly executed, and tumors were collected at 6 h after administration. Isolated tumors were fixed in 4% paraformaldehyde and prepared as paraffin sections. FITC-CD31was used to label tumor vessels, and 4′,6-diamidino-2-phenylindole (DAPI) was used to stain the nuclei. The untreated tumor was used as a blank control to deduct the autofluorescent background. Observation slides were used for immunofluorescence observation and analysis using a Pannoramic P250 digital section scanner (3D HISTECH, Budapest, Hungary).

In Vivo Photothermal Evaluation. When the H22 tumor volume increased to 200 mm^3, the mice were administered the drug intravenously, respectively. The mice were randomly divided into four groups (n = 5 per group) and treated under one of the following four experimental conditions: i.v. injected with NS only was defined as NS (−); treated with NS and exposed to the laser was defined as NS (+); treated with PB and exposed to the laser was defined as PB (+), 5 $\mu g/g$ body weight; and treated with PB/RHM and exposed to the laser was defined as PB/RHM (+), equivalent PB:5 $\mu g/g$ body weight. Mice were exposed to NIR 808 nm (1.25 W/cm^2) radiation for 10 min following administration for 6 h and were imaged and temperature was recorded by a thermal imager (FLIR ONE PRO, Teledyne FLIR).

Evaluation of Anti-Tumor Efficiency and Safety In Vivo. H22 cell-bearing mice were used as an animal model for *in vivo* anti-tumor evaluation. When the mean tumor volume reached 200 mm^3, the tumor-bearing mice were randomly grouped and treated in parallel with 6 mice in each group. The mice were treated under one of the following four experimental conditions: i.v. injected with NS only was defined as NS (−); treated with NS and exposed to the laser was defined as NS (+); treated with PB and exposed to the laser was defined as PB (+), 5 $\mu g/g$ body weight; and treated with PB/RHM and exposed to the laser was defined as PB/RHM (+), equivalent PB:5 $\mu g/g$ body weight. After 6 h of intravenous administration, the mice which required NIR radiation were treated with 10 min of NIR 808 nm radiation (1.25 W/cm^2). Subsequently, the body weight and tumor volume of the mice were continuously monitored and recorded for a fortnight. Following the last recording, surviving mice were euthanized, and tumors and other vital organs (heart, liver, spleen, lungs, kidneys) were collected. The isolated tumor was weighed precisely. The isolated tumors and other isolated organs were fixed in 4% paraformaldehyde and prepared as paraffin sections, which were then stained with hematoxylin and eosin (HE) according to a standard protocol. In addition, the isolated tumors were subjected to TUNEL staining and Ki67 immunohistochemistry to evaluate tumor tissue apoptosis, necrosis, and proliferation. Stained sections were examined histologically under a Pannoramic P250 digital section scanner (3D HISTECH, Budapest, Hungary). The tumor growth inhibition rate (TGI) was calculated according to eq 3:

$$TGI = (W_C - W_T)/W_C \times 100\% \quad (3)$$

where W_C denotes the tumor weight in the saline-treated control group and W_T represents the tumor weight after the specific treatment. All operational aspects of the animal experiments were followed in a double-blind manner.

Statistical Analysis. We used mean ± standard deviation (SD) to express the records, and statistical comparisons were made by one-way analysis of Variance (ANOVA) for multiple comparisons. $*p < 0.05$, $**p < 0.01$, and $***p < 0.001$ were considered statistically significant.

Data Availability. The data that support the findings of this study are available from the corresponding author upon reasonable request.

RESULTS AND DISCUSSION

Preparation and Characterization of PB/RHB. As illustrated in Figure 1, the PB/RHB construction process consisted of two sequential processes, PVP-modified PB synthesis and ultrasound-assisted hybrid membrane coating. PB is typically characterized by bare surface, heterogeneous nucleation, uncontrollable growth, and less uniform crystal size.[28] The addition of large amounts of PVP to the solution

https://doi.org/10.1021/acsomega.3c02370
ACS Omega 2023, 8, 23056−23066

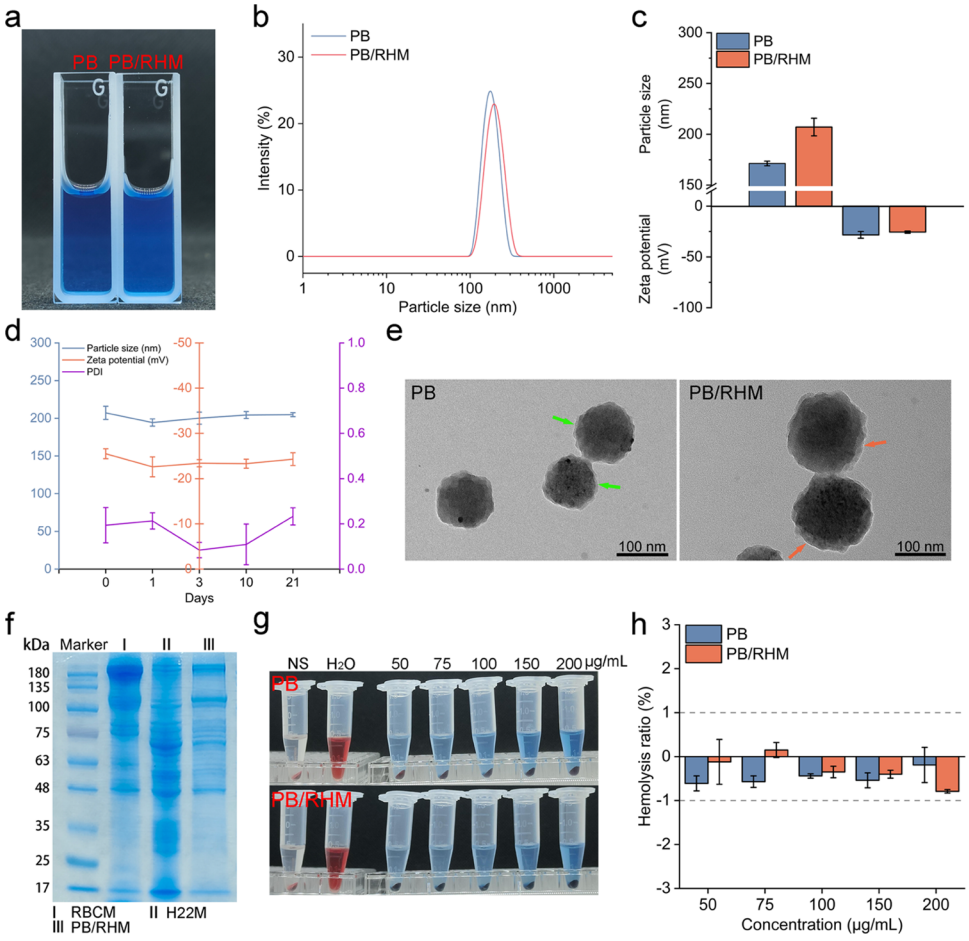

Figure 2. Characterizations of PB and PB/RHM. (a) Actual images of the aqueous dispersion of PB and PB/RHM. (b) Particle-size distribution of PB and PB/RHM obtained by DLS measurements (n = 3). (c) Size and ζ-potential analyses of PB and PB/RHM (n = 3). (d) Colloidal stability of PB/RHM. (e) TEM image of PB and PB/RHM. (f) Analysis of protein bands of RBCM, H22M, and PB/RHM by sodium dodecyl sulfate polyacrylamide gel electrophoresis (SDS-PAGE) and Coomassie brilliant blue staining. (g) Hemolysis photographs of PB and PB/RHM. (h) Hemolysis rates of PB and PB/RHM quantitatively assessed by measuring A540 (n = 3).

can assist in regulating the crystal growth of PB using a polymer permeation treatment strategy.[29] The carboxyl group of PVP can bind to Fe^{3+} at grain boundaries and crystal surfaces through the interaction of coordination reactions to passivate the grains, grain boundaries, and interfaces of the bulk phase, achieving homogeneous control of PB crystal growth and hydrophilic modification.[30] Subsequently, PB, erythrocyte membranes, and H22 tumor cell membranes were mixed together, and the cell membranes were reorganized and coated on the PB surface under the action of probe ultrasound to prepare PB/RHM.

As shown in Figure 2a, the aqueous dispersions of PB and PB/RHM were both clear blue systems at a concentration of 200 μg/mL, with the solution color PB/RHM being slightly lighter than PB. The results of the DLS measurements (Figure 2b,c) showed that the particle size of PB was 171.3 ± 2.3 nm, and the particle size of PB/RHM was 207.2 ± 8.7 nm. The increase in particle size of the PB after coating with the hybrid membrane was approximately 35 nm, suggesting that the hybrid membrane was successfully coated on the PB surface.[22,24] The ζ-potential of PB was −28.3 ± 3.3 mV and that of PB/RHM was −25.5 ± 1.1 mV. The negative surface potential of nanoformulations is of key critical importance to ensure their blood circulation stability and safety. During the membrane coating process, the outer membrane of the cell membrane had a negative charge due to the abundant glycocalyx on the surface, which was strongly electrostatically repelled by the negative charge of the PB and therefore wrapped the nanoparticles through the inner membrane.[31] This wrapping mechanism ensured the physiological orientation of the outer membrane, thus preserving the functionality of the membrane proteins.[32] It is essential that the nanoformulations have good colloidal stability as a fundamental formulation property for clinical development.[33] Figure 2d shows the colloidal stability results for PB/RHM over a 21-day period. The results showed that PB/RHM exhibited excellent colloidal stability, with the particle size, ζ-potential, and PDI remaining stable. TEM observations of the nanoparticles are provided in Figure 2e. The microscopic morphology of PB was monodisperse spheres, and the PVP coating modification on the surface could be observed. The PB/RHM was also a monodisperse sphere, and the complete encapsulation of the PB by the RHM hybrid membrane coating could be clearly observed. The particle sizes of PB and PB/RHM observed by TEM were both approximately 70 nm smaller than those determined by DLS. This was mainly due to the difference in measurement methods, as the DLS measurements included the hydrated layer on the surface of the nanoparticles and the long chains of PVP in an extended state, whereas the TEM measurements measured the size of the nanoparticles after

https://doi.org/10.1021/acsomega.3c02370
ACS Omega 2023, 8, 23056−23066

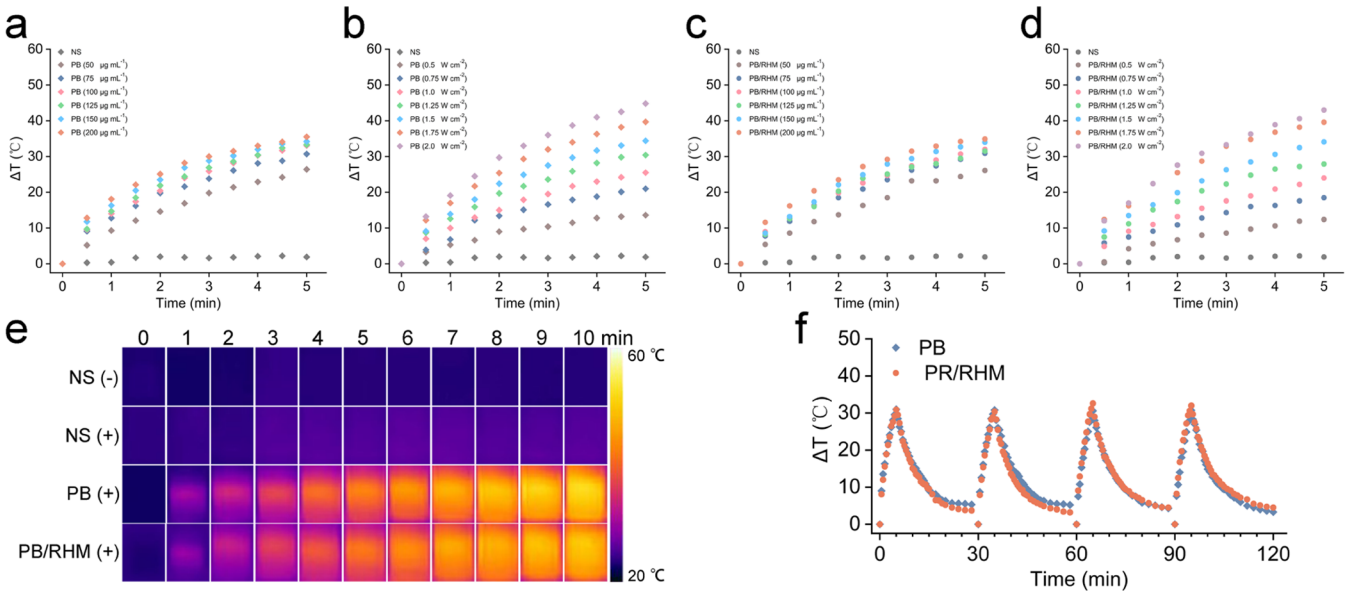

Figure 3. Photothermal properties of PB and PB/RHM. (a, c) Change curves of temperature of PB and PB/RHM aqueous dispersion with different concentrations under an irradiation of 808 nm, 1.25 W/cm^2 laser, respectively. (b, d) Change curves of temperature of PB and PB/RHM aqueous dispersion with different power densities under an irradiation of 808 nm, equivalent PB concentration: 100 μg/mL, respectively. (e) Thermal imaging photos of 1 mL of PB and PB/RHM aqueous dispersion under NIR irradiation (808 nm, 1.25 W/cm^2), equivalent PB concentration: 100 μg/mL. (f) Photothermal stability of PB and PB/RHM aqueous dispersion with four on/off cycles of (808 nm, 1.25 W/cm^2), equivalent PB concentration: 100 μg/mL.

drying and shrinking. The transfer of membrane proteins to the PB surface along with the lipid membrane was the most central aspect of the bionic functional modification of the nanoparticles by the membrane coating. Figure 2f demonstrates the results of the SDS-PAGE examination, and the protein bands of PB/RHM possessed the band characteristics of both RBCM and H22M, such as the characteristic bands between 75 and 100 kDa of RBCM and the characteristic bands between 48 and 75 kDa of H22M. This result indicated that PB/RHM effectively retained the membrane proteins of RBCM and H22M, providing the basis of formulation for the nanoparticles to achieve long circulation and tumor-homing targeting *in vivo*. The hemolytic evaluation provided a preliminary examination of the effect of nanoparticles on red blood cells and gave a judgment as to whether the formulation could be administered intravenously. As shown in Figure 2g,h, the hemolysis rate was less than 1% for both PB and PB/RHM in the concentration range of 50−200 μg/mL. The results indicated that PB and PB/RHM had no significant effect on the physiological status of red blood cells and could be used as an intravenous preparation for further *in vivo* biological studies.

***In Vitro* Evaluation of the Photothermal Properties of PB and PB/RHM.** Figure 3 shows the results of the *in vitro* photothermal evaluation of PB and PB/RHM. The photothermal properties relative to concentration for PB and PB/RHM are shown in Figure 3a,c. PB can warm up to 26.4 °C in 5 min at a concentration of 50 μg/mL, 33.1 °C at 100 μg/mL, and up to 35.5 °C at 200 μg/mL at a power density of 1.25 W/cm^2. These results indicated that PB had excellent photothermal properties with a significant concentration dependence. Compared to PB, the temperature rise of PB/RHM was similar to that of PB at each concentration, indicating that the hybrid membrane coating did not significantly affect the performance of PB in response to photothermal conversion by light radiation and that PB/RHM efficiently maintained the photothermal properties of PB. Figure 3b,d shows that the warming capacity of PB and PB/RHM was significantly related to the power density of the light radiation. PB and PB/RHM can both rise above 12 °C in 1 mL of aqueous solution at very low power densities (0.5 W/cm^2). At 2.0 W/cm^2, both nanoparticles achieved a warming capacity of more than 43 °C, demonstrating an excellent photothermal conversion capacity. Figure 3e provides a realistic view of the thermal images collected by the thermal infrared imager, demonstrating visually the superior photothermal conversion capability of the PB and PB/RHM. Good photothermal stability can provide assurance that the photothermal nanoparticles will exert their biological effects *in vivo*. Four cycles of photothermal radiation were executed for both PB and PB/RHM, and the results suggested that both PB and PB/RHM could maintain stable photothermal properties after several radiations. The fourth light radiation followed the same pattern of warming and cooling as the first light radiation, and the peak of warming could exceed 30 °C for all four cycles.

Evaluation of Cellular Uptake. The internalization of the nanoparticles by the target cells is a prerequisite for the function of the formulation.[34] The hybrid membrane was labeled with the lipophilic membrane dye DiO, and then the uptake of PB/RHM by H22 cells was visualized using fluorescence confocal techniques. As shown in Figure 4a, the distribution of the nanoparticle-labeled fluorescent signal within the H22 cells can be clearly observed. The blue signal of Hoechst 33342 labeling showed a large difference in the volume of the nuclei, which was due to the fact that the H22 cells were maintained in suspension, and the observation slides were prepared by dripping the cell suspension, which inevitably made it difficult to distribute the cells precisely in the same focal plane.

PTT-Induced Tumor Ablation *In Vitro*. A Hoechst 33342/PI double-staining assay was used to evaluate *in vitro*

https://doi.org/10.1021/acsomega.3c02370
ACS Omega 2023, 8, 23056−23066

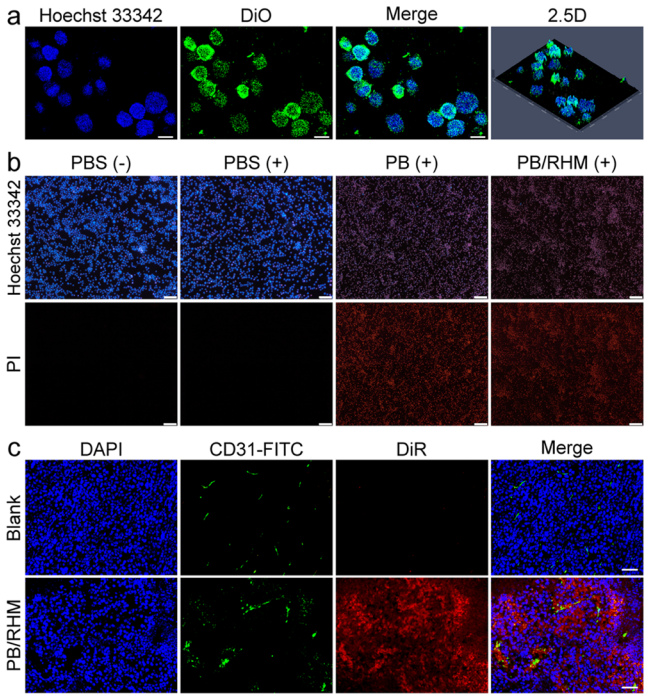

Figure 4. Cellular uptake, photothermal damage capacity *in vitro*, and tumor targeting *in vivo*. (a) CLSM images of intracellular distribution of PB/RHM after co-incubation with H22 cells for 12 h. Green: DiO-labeled RHM of PB/RHM; blue: Hoechst 33342-represented cell nuclei. Scar bar = 20 μm. (b) Hoechst 33342/PI staining assay for H22 cell after treatment with PBS, PB (100 μg/mL), and PB/RHM (equivalent PB concentration: 100 μg/mL) with laser irradiation (808 nm, 1.25 W/cm^2), scar bar = 200 μm. (c) Representative immunofluorescence images of the paraffin tissue sections of the tumor. Red: DiR-labeled RHM of PB/RHM; blue: DAPI-stained nuclei; green: FITC-CD31-labeled tumor blood vessels, scar bar = 100 μm.

the photothermal damage effect of PB and PB/RHM combined with NIR 808 nm radiation on H22 cells. As shown in Figure 4b, both the PBS (−) and PBS (+) groups were blue fluorescently labeled surviving cells, indicating that light radiation alone did not cause damage to H22 cells. The results for the PB (+) and PB/RHM (+) groups indicated that almost all cells were labeled with PI (red fluorescence), indicating that the cells were significantly damaged by the photothermal effect.

***In Vivo* Targeting Tumor Evaluation.** Nanoparticles need to overcome multiple barriers to accumulate in target tissues via blood circulation. The recognition and clearance mechanisms of the endothelial phagocytic system and the targeting ability of the nanoparticles are two of the most critical factors.[9] Biomimetic modification of nanoparticles by using erythrocyte membranes where the CD47 membrane protein on the surface can establish self-recognition communication with the phagocytic system and evade recognition, phagocytosis, and clearance, thus enhancing the long cycling capacity of the nanoparticles.[29] Functional modification of nanoparticles using tumor cell membranes can confer tumor homologous homing targeting capability to nanoparticles.[35] The lipophilic membrane dye DiR was used to label hybridized membranes, and the tumor-targeting accumulation capacity of PB/RHM was visualized using immunofluorescence observation techniques. Based on the results of previous studies, the nanoparticles modified with bionic coating can enter the accumulation plateau 6−8 h after intravenous administration, so we chose 6 h after tail vein administration as the observation time point for evaluating PB/RHM tumor-targeted accumulation.[27] As shown in Figure 4c, the observed field of view 6 h after tail vein administration showed abundant red fluorescence signals, indicating the efficient accumulation of the biomimetic photothermal nanoparticles PB/RHM into the tumor tissue. The efficient accumulation of PB/RHM in H22 tumor tissue offered the feasibility of nanoparticles for effective photothermal conversion and anti-tumor therapy *in vivo*.

***In Vivo* Photothermal Evaluation.** As the temperature of tumor cells reaches 45 °C, tumor necrosis can be induced by rapid thermal damage.[36−38] To evaluate the heating capacity of the biomimetic photothermal nanoparticles on the tumor region, NIR 808 nm light radiation was applied to the tumor region 6 h after tail vein administration, and direct observation and temperature tracking was performed using infrared thermography. Figure 5a shows images of the *in vivo* heating of the bionic photothermal nanoparticles, and Figure 5b shows the temperature change profile in the tumor region. The results of the NS (+) group showed that while the light radiation alone could heat up the target area, the temperature was below 42 °C, which did not cause significant biological effects, suggesting that the light radiation was safe for biological tissues. In the PB (+) group, the results showed that PB, as a superior photothermal material, would raise the temperature of the tumor area but could not achieve effective photothermal treatment of the tumor tissue due to its own low accumulation capacity in the tumor area. The PB/RHM (+) group demonstrated excellent photothermal properties. After 2 min of exposure to light radiation, the average temperature in the tumor area had reached 44.9 °C and continued to rise to 50.9 °C at 10 min. The excellent *in vivo* photothermal capacity of PB/RHM (+) was primarily due to the hybrid membrane bionic coating that efficiently enhanced the accumulation of photothermal nanoparticles in the tumor region. The continuous deposition of heat in the tumor region offered the possibility for anti-tumor therapy with biomimetic photothermal nanoparticles. In addition, the thermal imaging of the mice showed that the light radiation only induced local heating of the tumor area and did not have a significant thermal effect on other areas, which was crucial to improve the safety of the treatment.

Evaluation of Anti-Tumor Efficiency and Safety *In Vivo*. The *in vivo* anti-tumor evaluation of PB/RHM was carried out using H22 cell-bearing mice as the tumor model. Figure 5c shows the whole-mount images of each group of mice at the end of treatment, and Figure 5d provides a comparative view of the isolated tumors. Figure 5e,f shows the growth curve of each group of tumors over the treatment cycle. Similar tumor growth curves were observed in the NS (−) and NS (+) groups, where the mean tumor volumes at the end of treatment reached 2204 and 2225 mm^3, respectively, indicating that light radiation alone did not have a significant biological effect on tumor growth. Compared to the NS (+) group, the PB (+) group showed a degree of tumor inhibition. The mean tumor volume at 14 days was 1252 mm^3, and the tumor inhibition rate was 54.21%. The tumor growth trend was limited after the first treatment in the PB/RHM (+) group, and the tumor stopped growing and continued to ablate and decrease. At the endpoint of treatment, the tumor weight (Figure 5g) in the NS (−) group was 2.18 times higher than the PB group and 15.51 times higher than the PB/RHM (+)

https://doi.org/10.1021/acsomega.3c02370
ACS Omega 2023, 8, 23056−23066

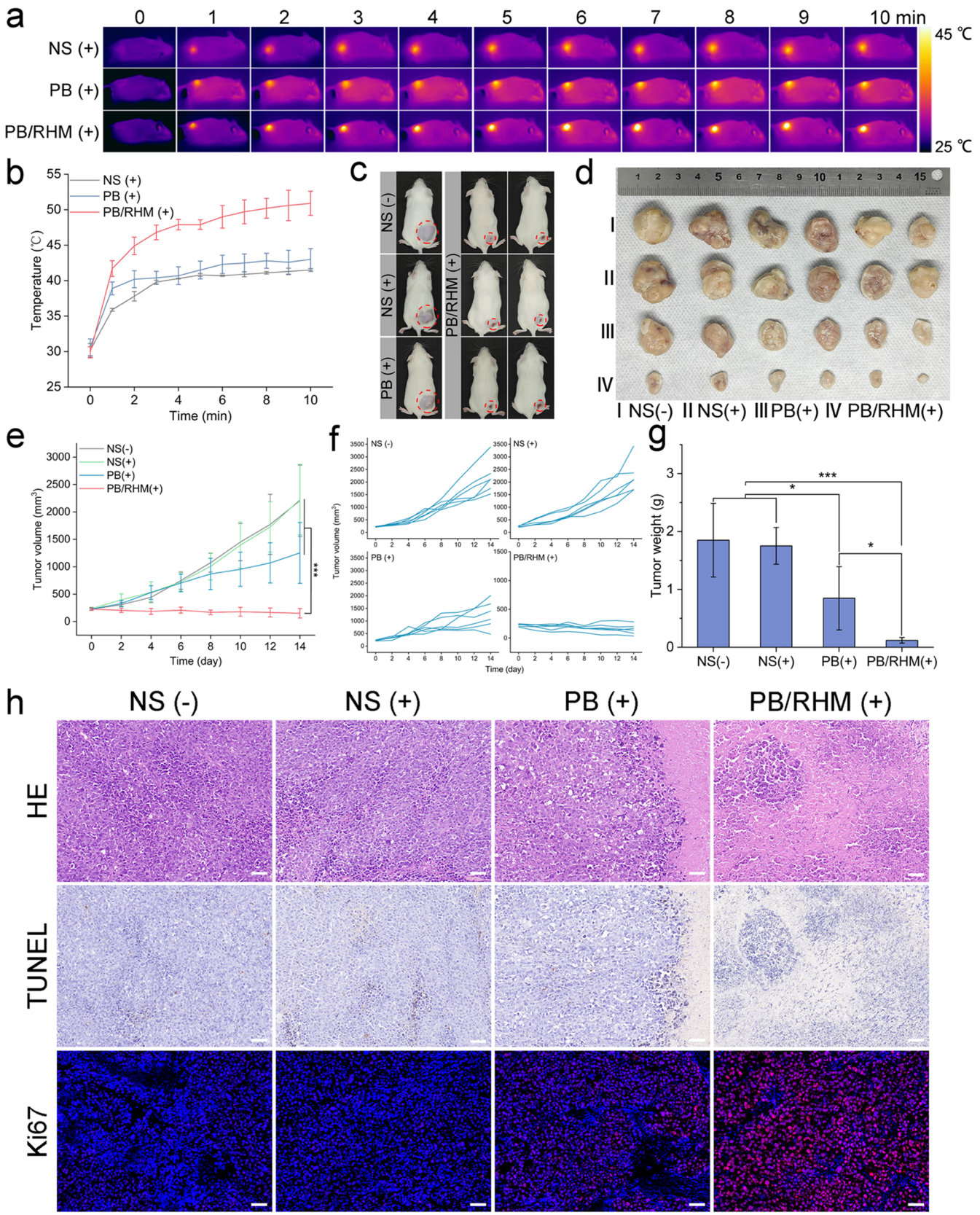

Figure 5. Photothermal effect and anti-tumor ability *in vivo*. (a) Thermal imaging of H22 cell-bearing mice in the NS (+), PB (+), and PB/RHM (+) groups. (b) Quantitative analysis of temperature. (c) Digital photos of the mice at the end of treatment. (d) Digital photos of tumors dissected from the sacrificed mice in NS (−), NS (+), PB (+), and PB/RHM (+) groups after 14 days of treatment. (e, f) Change in tumor volume over time for different treatment groups, $n = 6$. (g) Weight of isolated tumors, $n = 6$. Statistical significance was calculated via one-way ANOVA, giving p values, $^{*}p < 0.05$, $^{**}p < 0.01$, and $^{***}p < 0.001$. (h) Representative images of paraffin sections of tumor stained with hematoxylin−eosin (HE), TdT-mediated dUTP Nick-End Labeling (TUNEL), and Ki67 after treatment with different groups, scar bar = 100 μm.

https://doi.org/10.1021/acsomega.3c02370
ACS Omega 2023, 8, 23056−23066

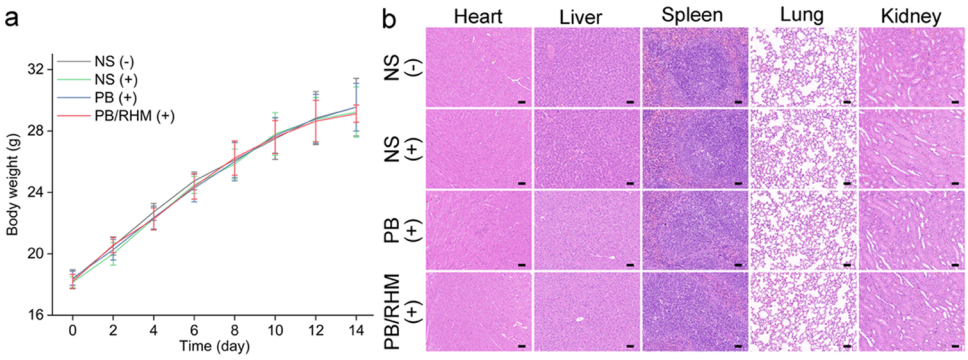

Figure 6. Safety evaluation. (a) Body weight changes of mice during the course of anti-tumor treatment, $n = 6$. (b) HE staining images of major organs (heart, liver, spleen, lung, and kidney) after different treatments.

group, respectively. A 93.56% tumor inhibition rate was achieved in the PB/RHM (+) group. The results of HE staining, TUNEL staining, and Ki67 staining for each group of tumors are shown in Figure 5h. Section images of the NS (−) and NS (+) groups showed good tumor tissue growth with no significant necrosis or apoptosis and were in an exuberant proliferative state. In the PB (+) group, partial necrosis of the tumor tissue was observed, but on the whole, the tumor was growing normally and proliferating. Observations in the PB/RHM (+) group indicated that the tumor tissue was heavily apoptotic or necrotic, with only a very small number of tumor cells in the proliferative state. These results suggested that PB/RHM combined with NIR 808 nm radiation could achieve effective anti-tumor therapy through efficient photothermal damage effects.

The body weight change curves (Figure 6a) of the mice showed steady growth in all groups without any drastic decrease in body weight. The HE staining results provided in Figure 6b show no significant organ damage in any of the groups of mice, suggesting that the bionic photothermal nano-delivery system provided a safe tumor treatment regimen. The biocompatibility of the constituent materials of the nano-formulations is the material basis for achieving *in vivo* therapeutic safety.[39] PB has been approved by the FDA, and RHM also has perfect biocompatibility as an endogenous biofilm material. In addition, the light radiation was precisely controlled in the tumor area and did not have a significant effect on the surrounding tissue. These two factors were the main reasons for the excellent safety of the bionic photothermal nano-delivery system.

CONCLUSIONS

Prussian blue nanoparticles were modified by hybridized membranes to be developed as a highly efficient bionic photothermal nano-delivery system for anti-tumor therapy. After the hybrid membrane coating, the bionic photothermal nanoparticles effectively retained the excellent photothermal properties of Prussian blue and had functional advantages of long circulation and tumor targeting, demonstrating efficient anti-tumor effects and satisfactory biocompatibility. In summary, PB/RHM could provide a new strategic option for anti-tumor research as a reliable bionic photothermal nano-delivery system.

AUTHOR INFORMATION

Corresponding Authors

Huichao Xie − *College of Pharmacy, Shenzhen Technology University, Shenzhen 518118, China;* orcid.org/0000-0002-4077-724X; Email: m18366133344@163.com

Tianyi Wang − *Ultrasound Department, First Affiliated Hospital of Jinzhou Medical University, Jinzhou 121001, China*; Email: 18104962111@163.com

Author

Zhining Liu − *Ultrasound Department, First Affiliated Hospital of Jinzhou Medical University, Jinzhou 121001, China*

Complete contact information is available at: https://pubs.acs.org/10.1021/acsomega.3c02370

Author Contributions

Z.L., H.X., and T.W. contributed to the conception of the study; Z.L. and H.X. performed the experiment; Z.L. and H.X. contributed significantly to analyses and manuscript preparation; Z.L. and H.X. performed the data analyses and wrote the manuscript; and T.W. helped perform the analysis with constructive discussions.

Notes

The authors declare no competing financial interest.

ACKNOWLEDGMENTS

This work was supported by the Nature Science Foundation of Liaoning (grant number 2022-MS-386) and Boze Young Scientific and Technological Talents Promotion Program of Jinzhou Medical University (grant number BZQT2107).

REFERENCES

(1) Pei, Q.; Hu, X.; Zheng, X.; Liu, S.; Li, Y.; Jing, X.; Xie, Z. Light-Activatable Red Blood Cell Membrane-Camouflaged Dimeric Prodrug Nanoparticles for Synergistic Photodynamic/Chemotherapy. *ACS Nano* **2018**, *12*, 1630−1641.

(2) Raguram, A.; Banskota, S.; Liu, D. R. Therapeutic in Vivo Delivery of Gene Editing Agents. *Cell* **2022**, *185*, 2806−2827.

(3) Mittelheisser, V.; Coliat, P.; Moeglin, E.; Goepp, L.; Goetz, J. G.; Charbonnière, L. J.; Pivot, X.; Detappe, A. Optimal Physicochemical Properties of Antibody−Nanoparticle Conjugates for Improved Tumor Targeting. *Adv. Mater.* **2022**, *34*, No. 2110305.

(4) Propper, D. J.; Balkwill, F. R. Harnessing Cytokines and Chemokines for Cancer Therapy. *Nat. Rev. Clin. Oncol.* **2022**, *19*, 237−253.

(5) Burgos-Morales, O.; Gueye, M.; Lacombe, L.; Nowak, C.; Schmachtenberg, R.; Hörner, M.; Jerez-Longres, C.; Mohsenin, H.;

Wagner, H. J.; Weber, W. Synthetic Biology as Driver for the Biologization of Materials Sciences. *Mater. Today Bio* **2021**, *11*, No. 100115.
(6) Meng, Q. Y.; Cong, H. L.; Hu, H.; Xu, F.-J. Rational Design and Latest Advances of Codelivery Systems for Cancer Therapy. *Mater. Today Bio* **2020**, *7*, No. 100056.
(7) Yang, Y.; Sun, B.; Zuo, S.; Li, X.; Zhou, S.; Li, L.; Luo, C.; Liu, H.; Cheng, M.; Wang, Y.; Wang, S.; He, Z.; Sun, J. Trisulfide Bond−Mediated Doxorubicin Dimeric Prodrug Nanoassemblies with High Drug Loading, High Self-Assembly Stability, and High Tumor Selectivity. *Sci. Adv.* **2020**, *6*, No. eabc1725.
(8) Xue, P.; Yang, R.; Sun, L.; Li, Q.; Zhang, L.; Xu, Z.; Kang, Y. Indocyanine Green-Conjugated Magnetic Prussian Blue Nanoparticles for Synchronous Photothermal/Photodynamic Tumor Therapy. *Nano-Micro Lett.* **2018**, *10*, 74.
(9) Zhang, Y.; Hao, S.; Zuo, J.; Guo, H.; Liu, M.; Zhu, H.; Sun, H. NIR-Activated Thermosensitive Liposome−Gold Nanorod Hybrids for Enhanced Drug Delivery and Stimulus Sensitivity. *ACS Biomater. Sci. Eng.* **2023**, *9*, 340−351.
(10) Pei, W.; Huang, B.; Chen, S.; Wang, L.; Xu, Y.; Niu, C. Platelet-Mimicking Drug Delivery Nanoparticles for Enhanced Chemo-Photothermal Therapy of Breast Cancer. *Int. J. Nanomed.* **2020**, *15*, 10151−10167.
(11) Zhu, X.; Chen, X.; Jia, Z.; Huo, D.; Liu, Y.; Liu, J. Cationic Chitosan@Ruthenium Dioxide Hybrid Nanozymes for Photothermal Therapy Enhancing ROS-Mediated Eradicating Multidrug Resistant Bacterial Infection. *J. Colloid Interface Sci.* **2021**, *603*, 615−632.
(12) Sahu, A.; Lee, J. H.; Lee, H. G.; Jeong, Y. Y.; Tae, G. Prussian Blue/Serum Albumin/Indocyanine Green as a Multifunctional Nanotheranostic Agent for Bimodal Imaging Guided Laser Mediated Combinatorial Phototherapy. *J. Controlled Release* **2016**, *236*, 90−99.
(13) Peng, J.; Yang, Q.; Li, W.; Tan, L.; Xiao, Y.; Chen, L.; Hao, Y.; Qian, Z. Erythrocyte-Membrane-Coated Prussian Blue/Manganese Dioxide Nanoparticles as H 2 O 2 -Responsive Oxygen Generators to Enhance Cancer Chemotherapy/Photothermal Therapy. *ACS Appl. Mater. Interfaces* **2017**, *9*, 44410−44422.
(14) Hannah, A.; Luke, G.; Wilson, K.; Homan, K.; Emelianov, S. Indocyanine Green-Loaded Photoacoustic Nanodroplets: Dual Contrast Nanoconstructs for Enhanced Photoacoustic and Ultrasound Imaging. *ACS Nano* **2014**, *8*, 250−259.
(15) Su, Y. Y.; Jiang, X. Y.; Zheng, L. J.; Yang, Y. W.; Yan, S. Y.; Tian, Y.; Tian, W.; Liu, W. F.; Teng, Z. G.; Yao, H.; Wang, S. J.; Zhang, L. J. Hybrid Au-Star@Prussian Blue for High-Performance towards Bimodal Imaging and Photothermal Treatment. *J. Colloid Interface Sci.* **2023**, *634*, 601−609.
(16) Lu, L.; Zhang, C.; Zou, B.; Wang, Y. Hollow Prussian Blue Nanospheres for Photothermal/Chemo-Synergistic Therapy. *Int. J. Nanomed.* **2020**, *15*, 5165−5177.
(17) Wang, Z.; Long, Y.; Fan, J.; Xiao, C.; Tong, C.; Guo, C.; Chen, X.; Liu, B.; Yang, X. Biosafety and Biocompatibility Assessment of Prussian Blue Nanoparticles in Vitro and in Vivo. *Nanomedicine* **2020**, *15*, 2655−2670.
(18) Cahu, M.; Ali, L. M. A.; Sene, S.; Long, J.; Camerel, F.; Ciancone, M.; Salles, F.; Chopineau, J.; Devoisselle, J.-M.; Felix, G.; Cubedo, N.; Rossel, M.; Guari, Y.; Bettache, N.; Larionova, J.; Gary-Bobo, M. A Rational Study of the Influence of Mn 2+ -Insertion in Prussian Blue Nanoparticles on Their Photothermal Properties. *J. Mater. Chem. B* **2021**, *9*, 9670−9683.
(19) Li, Z. H.; Chen, Y.; Sun, Y.; Zhang, X. Z. Platinum-Doped Prussian Blue Nanozymes for Multiwavelength Bioimaging Guided Photothermal Therapy of Tumor and Anti-Inflammation. *ACS Nano* **2021**, *15*, 5189−5200.
(20) Fang, R. H.; Gao, W.; Zhang, L. Targeting Drugs to Tumours Using Cell Membrane-Coated Nanoparticles. *Nat. Rev. Clin. Oncol.* **2023**, *20*, 33−48.
(21) Liu, L.; Pan, D.; Chen, S.; Martikainen, M.-V.; Kårlund, A.; Ke, J.; Pulkkinen, H.; Ruhanen, H.; Roponen, M.; Käkelä, R.; Xu, W.; Wang, J.; Lehto, V.-P. Systematic Design of Cell Membrane Coating to Improve Tumor Targeting of Nanoparticles. *Nat. Commun.* **2022**, *13*, No. 6181.
(22) Yang, Z.; Gao, D.; Guo, X.; Jin, L.; Zheng, J.; Wang, Y.; Chen, S.; Zheng, X.; Zeng, L.; Guo, M.; Zhang, X.; Tian, Z. Fighting Immune Cold and Reprogramming Immunosuppressive Tumor Microenvironment with Red Blood Cell Membrane-Camouflaged Nanobullets. *ACS Nano* **2020**, *14*, 17442−17457.
(23) Guo, Y.; Wang, D.; Song, Q.; Wu, T.; Zhuang, X.; Bao, Y.; Kong, M.; Qi, Y.; Tan, S.; Zhang, Z. Erythrocyte Membrane-Enveloped Polymeric Nanoparticles as Nanovaccine for Induction of Antitumor Immunity against Melanoma. *ACS Nano* **2015**, *9*, 6918−6933.
(24) Zeng, Y.; Li, S.; Zhang, S.; Wang, L.; Yuan, H.; Hu, F. Cell Membrane Coated-Nanoparticles for Cancer Immunotherapy. *Acta Pharm. Sin. B* **2022**, *12*, 3233−3254.
(25) Zhao, X.; Yan, C. Research Progress of Cell Membrane Biomimetic Nanoparticles for Tumor Therapy. *Nanoscale Res. Lett.* **2022**, *17*, 36.
(26) Jiang, Q.; Liu, Y.; Guo, R.; Yao, X.; Sung, S.; Pang, Z.; Yang, W. Erythrocyte-Cancer Hybrid Membrane-Camouflaged Melanin Nanoparticles for Enhancing Photothermal Therapy Efficacy in Tumors. *Biomaterials* **2019**, *192*, 292−308.
(27) Xie, H.; Li, W.; Liu, H.; Chen, Y.; Ma, M.; Wang, Y.; Luo, Y.; Song, D.; Hou, Q.; Lu, W.; Bai, Y.; Li, B.; Ma, J.; Huang, C.; Yang, T.; Liu, Z.; Zhao, X.; Ding, P. Erythrocyte Membrane-Coated Invisible Acoustic-Sensitive Nanoparticle for Inducing Tumor Thrombotic Infarction by Precisely Damaging Tumor Vascular Endothelium. *Small* **2022**, *18*, No. 2201933.
(28) Fu, J.; Wu, B.; Wei, M.; Huang, Y.; Zhou, Y.; Zhang, Q.; Du, L. Prussian Blue Nanosphere-Embedded in Situ Hydrogel for Photothermal Therapy by Peritumoral Administration. *Acta Pharm. Sin. B* **2019**, *9*, 604−614.
(29) Liu, B.; Wang, W.; Fan, J.; Long, Y.; Xiao, F.; Daniyal, M.; Tong, C.; Xie, Q.; Jian, Y.; Li, B.; Ma, X.; Wang, W. RBC Membrane Camouflaged Prussian Blue Nanoparticles for Gamabutolin Loading and Combined Chemo/Photothermal Therapy of Breast Cancer. *Biomaterials* **2019**, *217*, No. 119301.
(30) Peng, X.; Wang, R.; Wang, T.; Yang, W.; Wang, H.; Gu, W.; Ye, L. Carbon Dots/Prussian Blue Satellite/Core Nanocomposites for Optical Imaging and Photothermal Therapy. *ACS Appl. Mater. Interfaces* **2018**, *10*, 1084−1092.
(31) Xiong, J.; Wu, M.; Chen, J.; Liu, Y.; Chen, Y.; Fan, G.; Liu, Y.; Cheng, J.; Wang, Z.; Wang, S.; Liu, Y.; Zhang, W. Cancer-Erythrocyte Hybrid Membrane-Camouflaged Magnetic Nanoparticles with Enhanced Photothermal-Immunotherapy for Ovarian Cancer. *ACS Nano* **2021**, *15*, 19756−19770.
(32) Yu, H.; Fan, J.; Shehla, N.; Qiu, Y.; Lin, Y.; Wang, Z.; Cao, L.; Li, B.; Daniyal, M.; Qin, Y.; Peng, C.; Cai, X.; Liu, B.; Wang, W. Biomimetic Hybrid Membrane-Coated Xuetongsu Assisted with Laser Irradiation for Efficient Rheumatoid Arthritis Therapy. *ACS Nano* **2022**, *16*, 502−521.
(33) Daniyal, M.; Jian, Y.; Xiao, F.; Sheng, W.; Fan, J.; Xiao, C.; Wang, Z.; Liu, B.; Peng, C.; Yuhui, Q.; Wang, W. Development of a Nanodrug-Delivery System Camouflaged by Erythrocyte Membranes for the Chemo/Phototherapy of Cancer. *Nanomedicine* **2020**, *15*, 691−709.
(34) Gao, Y.; Zhao, J.; Huang, Z.; Zhao, H.; Guo, Z.; Ma, S.; Tang, X.; Song, W.; Chen, X. In Situ Reprogramming of Tumors for Activating the OX40/OX40 Ligand Checkpoint Pathway and Boosting Antitumor Immunity. *ACS Biomater. Sci. Eng.* **2022**, No. 01637.
(35) Wang, C.; Wu, S. Research Update on Cell Membrane Camouflaged Nanoparticles for Cancer Therapy. *Front. Bioeng. Biotechnol.* **2022**, *10*, No. 944518.
(36) Pang, H.; Tian, C.; He, G.; Zhang, D.; Yang, J.; Zhang, Q.; Liu, R. NIR-Absorbing Prussian Blue Nanoparticles for Transarterial Infusion Photothermal Therapy of VX2 Tumors Implanted in Rabbits. *Nanoscale* **2021**, *13*, 8490−8497.

https://doi.org/10.1021/acsomega.3c02370
ACS Omega 2023, 8, 23056−23066

(37) Zhang, K.; Li, D.; Zhou, B.; Liu, J.; Luo, X.; Wei, R.; Wang, L.; Hu, X.; Su, Z.; Lin, H.; Gao, J.; Shan, H. Arsenite-Loaded Albumin Nanoparticles for Targeted Synergistic Chemo-Photothermal Therapy of HCC. *Biomater. Sci.* **2021**, *10*, 243−257.
(38) Wu, W.; Yu, L.; Pu, Y.; Yao, H.; Chen, Y.; Shi, J. Copper-Enriched Prussian Blue Nanomedicine for In Situ Disulfiram Toxification and Photothermal Antitumor Amplification. *Adv. Mater.* **2020**, *32*, No. 2000542.
(39) Liu, Y.; Yang, Y.; Sun, M.; Cui, M.; Fu, Y.; Lin, Y.; Li, Z.; Nie, L. Highly Specific Noninvasive Photoacoustic and Positron Emission Tomography of Brain Plaque with Functionalized Croconium Dye Labeled by a Radiotracer. *Chem. Sci.* **2017**, *8*, 2710−2716.

https://doi.org/10.1021/acsomega.3c02370
ACS Omega 2023, 8, 23056−23066